Effect of Fence on Linear Aerospike Plume-Induced Base-Heating Physics

Ten-See Wang*

NASA Marshall Space Flight Center, Huntsville, Alabama 35812

A computational heat transfer analysis is conducted to study the effect of the presence of an engine fence on the X-33 linear aerospike plume-induced base heating during vehicle ascent. A fence is an extension of the plug side wall that reduces the plume spillage. A detailed three-dimensional thermoflowfield of the entire vehicle is computed such that an accurate freestream flow environment is assured for the base-flow development. The computational methodology is based on a finite difference, viscous flow, chemically reacting, pressure-based computational fluid dynamics formulation and a finite volume, spectral-line-based weighted sum of gray gases absorption computational radiation heat transfer formulation. The computed base-flow physics are analyzed and compared with those of a subscale model hot-flow test. The effect of base bleed is also analyzed.

Nomenclature

C_1, C_2, C_3, C_μ	=	turbulence modeling constants: 1.15, 1.9, 0.25, and 0.09, respectively
G	=	geometrical metrices
H	=	total enthalpy
h	=	static enthalpy or altitude, km
I	=	radiative intensity
J	=	Jacobian of coordinate transformation
K	=	forward rate constant
k	=	turbulent kinetic energy
M	=	Mach number
N	=	total number of chemical species
P	=	pressure
PC	=	combustion chamber pressure
Pr	=	Prandtl number
Q	=	heat flux, kW/m^2
q	=	1, $u, v, w, H, k, \varepsilon$, or ρ_i
R	=	recovery factor
r	=	location coordinate
S_q	=	source term for equation q
T^+	=	law of the wall temperature
t	=	time, s
U	=	volume-weighted contravariant velocity
u, v, w	=	mean velocities in three directions
u_τ	=	wall friction velocity
u^+	=	law of the wall velocity, u/u_τ
x, y, z	=	coordinate or distance
y^+	=	law of the wall distance, $(y_p u_\tau \rho / \mu)$
ε	=	turbulent kinetic energy dissipation rate or wall emissivity
κ	=	absorption coefficient
μ	=	effective viscosity, $\mu_l + \mu_t$
ξ	=	computational coordinates
Π	=	turbulent kinetic energy production
ρ	=	density
σ_q	=	turbulence modeling constants
φ	=	energy dissipation function
Ω	=	direction vector
ω	=	chemical species production rate

Subscripts

a	=	ambient
b	=	blackbody or base
c	=	convective or center
l	=	laminar flow
p	=	off-wall (wall function) point
r	=	radiative
t	=	turbulent flow
w	=	wall surface
0	=	reference
∞	=	freestream

Introduction

THE X-33 is a single-stage-to-orbit advanced technology demonstrator to be built by Lockheed Martin Skunk Works for NASA's reusable launch vehicle (RLV) program. This half-scale prototype of a rocket-based system is fueled by liquid hydrogen and liquid oxygen and features a lifting body configuration, coupled with two integrated, linear aerospike rocket engines to propel the vehicle.

It is widely recognized that aerospike engines have the potential advantage of adjusting themselves to perform with maximum efficiency at all altitudes.[1,2] However, the hot aerospike plume-induced base-heating physics are not as well understood. In addition, the plume spillage from an unfenced engine ramp represents a performance loss, and the resulting lateral plume jet impingement on the base components creates a potential higher heating environment. Reference 3 developed a three-dimensional computational methodology to examine the X-33 base-flow physics for an unfenced engine ramp at several altitudes. The computed base-flow properties, although not directly compared with a measurement (because none was available), showed several important aspects of the base-heating physics. In this study, the computed base-heating physics are further examined with a composite graphics method that includes the fence effect. Furthermore, to verify the computed base-heating physics, the computed base-flow properties are compared with those of a recently available subscale model of a hot-fire test.[4,5]

Solution Methodology

Computational Grid Generation

Figure 1 shows the layout of a typical X-33 surface computational grid. In addition to all other body components, the key feature of the X-33 is the aerospike's unique inside out nozzle, which consists of two ramps oriented to the upper and lower surfaces of the
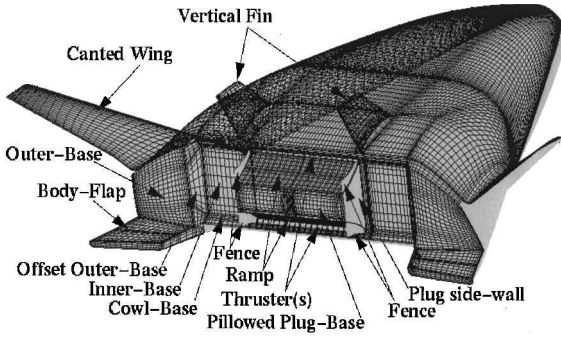
Fig. 1   Layout of an X-33 surface computational grid with fence.

vehicle. Two banks of 20 thrust cells line the ends of each side of the nozzle along the vehicle-to-engine interface. The fence is seen erected on the sides of the ramp. The primary flow is exhausted from the thrust cells and expanded against the nozzle ramp surfaces to provide the major portion of the engine thrust. In actual calculations, only one-half of the domain is used, assuming flow symmetry. The computational grid used in this study was gradually improved through a sequential grid-refinement technique.[3] That is, not only was the grid density increased from 1,803,614 points to the eventual 2,217,444 points using a patched-grid method, but the grid distribution was enhanced through a solution-adaptive grid method as well. Details of the sequential grid-refinement technique can be found in Ref. 3. The basic algebraic grid is generated with the software package GRIDGEN.[6] A self-adaptive grid code (SAGEv2)[7] is then used to redistribute the points. This sequential grid-refinement strategy allows the full-vehicle base-flow physics to be computed in an efficient manner.

Thermal Environment Computation

Two computational methodologies are used to perform the computational heat transfer analysis: the finite difference Navier–Stokes (FDNS) computational fluid dynamics (CFD) code[8,9] for the convective heating and the general radiation solution program (GRASP)[10] for the radiative heating. These tools have been developed at NASA Marshall Space Flight Center (MSFC) and are continuously being improved by MSFC personnel and its support contractors. Systematic and rigorous benchmark studies have been performed for rocket base-flow and heat transfer applications.[11–16] In this study, FDNS and GRASP calculations are conducted sequentially to save computer resources. The CFD computed pressure, H_2O concentration, and temperature fields are used as input for the radiation calculations. The solution algorithm for the thermal environment computation is summarized in the following.

Convective Heat Transfer

FDNS solves a general curvilinear coordinate, chemically reacting, viscous thermo-flowfield with Reynolds-averaged transport equations. A generalized form of these equations is given by

$$\frac{\partial \rho q}{J \partial t} = \frac{\partial[-\rho Uq + (\mu/\sigma_q)G(\partial q/\partial \xi)]}{\partial \xi} + \frac{S_q}{J} \qquad (1)$$

A pressure-based predictor plus multicorrector solution method is used.[17] The basic idea is to perform correction for the pressure and velocity fields by solving for a pressure correction so that the velocity–pressure coupling is enforced based on the continuity constraint. A second-order central-difference scheme is employed to discretize the diffusion fluxes and source terms of the governing equations. For the convective terms, a second-order total variation diminishing difference scheme is used in this effort.

An extended k–ε turbulence model[18] is used to describe the turbulence, and $\mu_t = \rho C_\mu k^2/\varepsilon$ is defined as the turbulence eddy viscosity. Turbulence modeling constants σ_q and source terms S_q of the transport equations are given in Table 1. These turbulence

Table 1   Constants σ_q and source terms S_q of the transport equations

q	σ_q	S_q
1	1.00	0
u	1.00	$-P_x + \nabla[\mu(u_j)_x] - \frac{2}{3}(\mu \nabla u_j)_x$
v	1.00	$-P_y + \nabla[\mu(u_j)_y] - \frac{2}{3}(\mu \nabla u_j)_y$
w	1.00	$-P_z + \nabla[\mu(u_j)_z] - \frac{2}{3}(\mu \nabla u_j)_z$
H	0.90	$DP/DT + \varphi$
k	0.89	$\rho(\Pi - \varepsilon)$
ε	1.15	$\rho(\varepsilon/k)\{[C_1 + C_3(\Pi/\varepsilon)]\Pi - C_2\varepsilon\}$
ρ_i	0.90	$\omega_i, i = 1, \ldots, N$

Table 2   Hydrogen/oxygen combustion kinetics mechanism

Reaction[a]	A	B	E/R
$H_2 + O_2 = OH + OH$	$1.700E13$	0	$2.407E4$
$OH + H_2 = H_2O + H$	$2.190E13$	0	$2.590E3$
$OH + OH = O + H_2O$	$6.023E12$	0	$5.500E2$
$O + H_2 = H + OH$	$1.800E10$	1.0	$4.480E3$
$H + O_2 = O + OH$	$1.220E17$	-0.91	$8.369E3$
$M + O + H = OH + M$	$1.000E16$	0	0
$M + O + O = O_2 + M$	$2.550E18$	-1.0	$5.939E4$
$M + H + H = H_2 + M$	$5.000E15$	0	0
$M + H + OH = H_2O + M$	$8.400E21$	-2.0	0

[a]M stands for third-body collision partner and $K = AT^B e^{-E/RT}$.

modeling constants have been used extensively for combustion-driven and base flows,[11–17,19] whereas σ_k and σ_ε are taken from the turbulence closure.[18] A seven-species, nine-reaction detailed mechanism[19] (Table 2) is used to describe the finite rate hydrogen/oxygen afterburning chemical kinetics. The seven species are H_2, O_2, H_2O, O, H, OH, and N_2, where H_2O is the major radiating medium.

A modified wall function approach is employed to provide wall boundary-layer solutions that are less sensitive to the near-wall grid spacing. The model has combined the advantages of both the integrated to the wall approach and the conventional law of the wall approach by incorporating a complete velocity profile[20] given by

$$u^+ = \left[(y^+ + 11)^{4.02}\Big/\left(y^{+2} - 7.37y^+ + 83.3\right)^{0.79}\right]$$
$$+ 5.63 \tan^{-1}(0.12y^+ - 0.441) - 3.81 \qquad (2)$$

and a universal temperature profile[21] given by

$$T^+ = u^+ + 12.8\left(Pr_l^{0.68} - 1\right) \qquad (3)$$

The convective heat transfer from a hot boundary layer to a cooler wall follows the modified Newtonian law[16]

$$Q_{cw} = \left(\rho u_\tau/T^+\right)\left[h_w - h_p - R\left(u_p^2/2\right)\right] \qquad (4)$$

where $R = Pr_l^{1/2}$ if $y^+ \leq 11.63$ and $R = Pr_l^{1/3}$ if $y^+ > 11.63$ and where $y^+ = 11.63$ is the thickness of the viscous sublayer. A constant Pr_l of air is used in this study, because parametric studies performed in Ref. 16 show that the H_2/O_2 plume-induced base heat flux is not sensitive to a multicomponent variable Pr_l.

Radiative Heat Transfer

GRASP analyzes the radiative field by solving the general curvilinear coordinate radiative transfer equation with a finite volume method (FVM) formulation[22]:

$$(\Omega \cdot \nabla)I(r, \Omega) = -\kappa I(r, \Omega) + \kappa I_b(r) \qquad (5)$$

The term on the left-hand side represents the gradient of the intensity in the direction of Ω. The two terms on the right-hand side represent the changes in intensity due to absorption and emission. The wall boundary is assumed gray while emitting and reflecting diffusely, and the radiative wall boundary condition is given by

$$I\left(r_w, \Omega^+\right) = \varepsilon I_b(r_w) + \frac{(1 - \varepsilon)}{\pi} \int\limits_{n \cdot \Omega^- < 0} I\left(r_w, \Omega^-\right) |n \cdot \Omega^-| \, d\Omega^- \tag{6}$$

with

$$q_{rw} = \int\limits_{n \cdot \Omega^- < 0} I\left(r_w, \Omega^-\right) |n \cdot \Omega^-| \, d\Omega^- \tag{7}$$

where Ω^+ and Ω^- denote the leaving and arriving radiative intensity directions, respectively. The 20-band spectral-line weighted sum of gray gases model[10] is used to calculate the total emissivity and absorptivity of the radiating medium. Following the ray-dependency test performed in Ref. 16, the FVM 6 × 4 option, six control angles in the polar direction and four in the azimuthal direction, is deemed adequate and used in this effort.

Boundary and Initial Conditions

The outer boundary of the computational domain is bounded by the fixed total condition (freestream) boundaries, one symmetry plane, and the flow exit plane. A no-slip wall is specified for the body surface. A fixed (ambient) static pressure is imposed on the exit plane and on a point far away from the action area (one grid point off of the freestream boundary) to obtain a unique solution for the desired altitude. The fixed inlet boundary condition is applied to the multiple-thruster exit plane where the flow properties are mapped from a separate three-dimensional single-thruster solution to ensure proper nozzle exhaust flow properties for the plume-induced base environment calculations.[15] The single thruster has a circular cross-sectional chamber and transforms to a rectangular nozzle.[3] The subsonic chamber inlet-flow properties were obtained from a thermoequilibrium analysis[23] using engine conditions. This procedure of performing a separate thrust chamber calculation is important to the final solution[15] because the propulsive nozzle flow is the major driver for the ensuing base-flow physics. For the base-bleed flow on the plug base, a fixed mass flow rate (and energy) boundary condition is used in the subsonic freestream cases and a fixed inlet boundary condition is applied in the supersonic freestream cases.

For convective heat transfer calculations, ambient temperature is prescribed for the forebody and aftbody surface, whereas 540 deg R is specified for all base surfaces per base-heating design convention. For radiation calculations, the surface emissivity of the entire vehicle is assumed to be 0.7 (Ref. 16). The engine ramp is actively cooled and the surface temperature distribution is prescribed from a separate conjugate heat transfer calculation involving solid walls and coolant channel flows.[3] It was found that cowl-base irradiation is more than ten times higher if adiabatic condition is imposed on the ramp surface.[3] Hence, a more accurate prescribed temperature boundary condition is employed. Notice that the effect of reirradiation from surface radiation is included in all of the calculations.

Results and Discussion

The flow computations were performed on a NASA MSFC 16-processor Silicon Graphics Power Challenge. The computational time for a typical frozen chemistry (fixed plume composition) calculation is estimated as 4.5×10^{-6} CPU s/grid/step, whereas the computational time for a typical finite rate chemistry calculation is 1.5×10^{-5} CPU s/grid/step. Usually, 1000–3000 iterations are required to achieve a converged solution. The convergence is achieved when all of the residuals dropped at least six orders of magnitude and flow properties monitored at several strategic locations reached approximate steady state. The radiation computations were performed on the NASA MSFC J-90 Cray, where the computational time for a typical run is approximately 6.5×10^{-5} CPU s/grid/step/direction and typically 20 iterations are needed.

The finding of diminishing plume afterburning due to air dilution and shortened residence time at high altitudes and supersonic freestreams[3] allows the frozen flow chemistry to be used for supersonic trajectory computations, whereas the finite rate chemistry

Table 3 Trajectory conditions

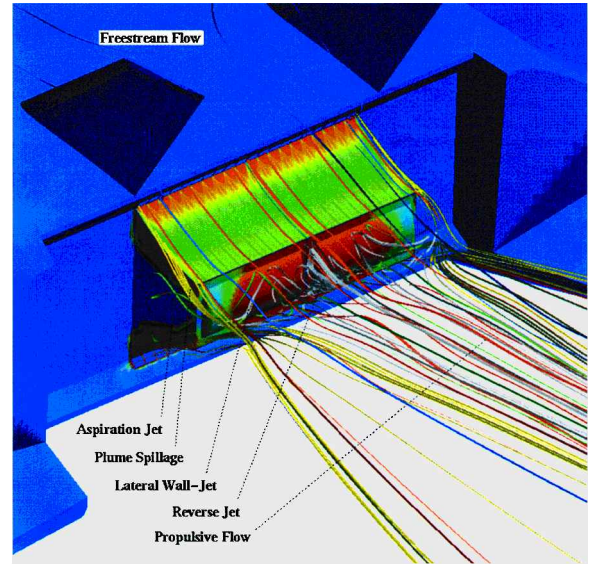| PC, Pa	M_∞	h
63	0.00	0.7
92	0.60	3.7
510	1.72	15.3
1804	2.81	23.4
5790	4.07	31.1

Fig. 2   Base convective heat-flux and streamline contours for baseline case at 0.7 km.

option is applied to the subsonic trajectory points. This frozen chemistry assumption leads to a reduction of the participating species number from seven to a maximum of three (air, plume, and base bleed). Notice that the species air, plume, and base bleed are composite species. For example, the molecular weight and thermodynamics of composite-species air are those derived from 21% (molar) oxygen and 79% nitrogen using a simple mixing rule. In all, results from fifteen three-dimensional flight model computations, baseline (without base bleed and fence), base-bleed (without fence), and base-bleed with fence cases at five altitudes, are used to infer the linear aerospike plume-induced base-heating physics during powered flight. Also note that the computed forebody and aftbody surface pressure coefficients agreed reasonably well with those of a 7.75% scaled cold-flow model test,[3] indicating the incoming flow environment is adequately simulated for the base-flow development. Table 3 shows the assumed trajectory conditions for the flight simulation.

An earlier study[3] indicated that the linear aerospike plume-induced base flow is not only complicated but also three-dimensional. To understand the resulting base-heating physics, a composite postprocessing graphics method is devised to interrogate the computed thermoflowfields. This involves superimposing streamlines with particles released at selected strategic locations onto surface convective heat flux contours, as shown in Figs. 2–4. To accentuate the individual base thermoflow physics occurring in different base regions, three maximum scales (kilowatts per square meter) are used for the convective heating contours: ramp, 0–9000; plug-base, 0–400; and remainder, 0–60. In addition, to better differentiate the streamlines that represent different flow physics at different trajectory points and different design conditions, five color streamline groups are used: blue, representing freestream flows; red, representing propulsive flows originating from the thrusters flowing near the ramp surface; gray, representing recirculating flows, reverse-jet, and wall-jet flowing inside the prism-shaped dome formed by the plume flows and the plug-base pillows; green, representing aspirating flows and recirculating flows originating near the surfaces of inner and outer bases; and yellow, representing plume spillage coming off of
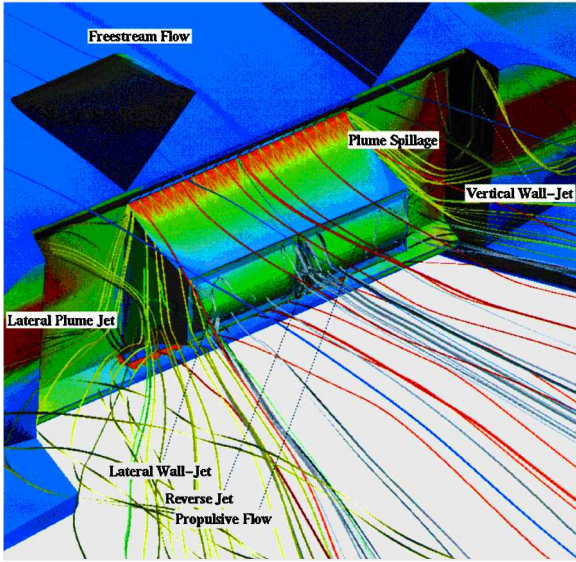
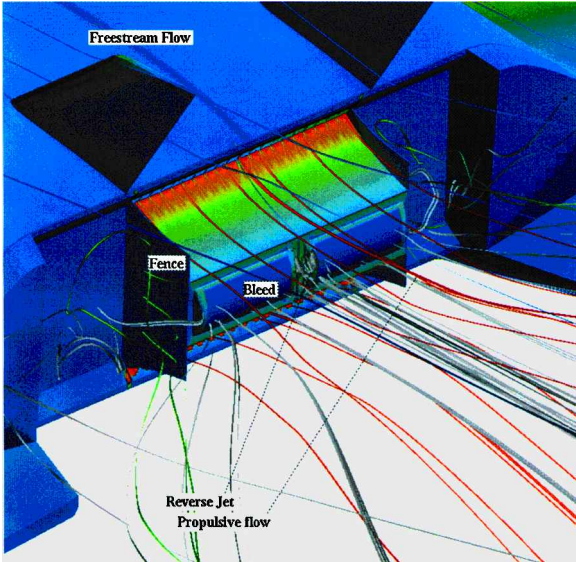**Fig. 3   Base convective heat-flux and streamline contours for baseline case at 23.4 km.**

Fig. 4   Base convective heat-flux and streamline contours for base-bleed with fence case at 31.1 km.

the ramp edge and eventually becoming the lateral plume jet at high altitudes. Selected results are shown in Figs. 2–4 and the inferred physics are discussed next.

Base-Heating Physics from Computational Flight Simulations

Figure 2 shows the computed base-heating physics for the baseline case at 0.7 km. The upper- and lower-engine propulsive flows (plumes) speed down the ramps and appear to merge at a short distance after the plug base, whereas the reverse jet develops (see the double-triangle recirculation formation at the plug-base center). The free shear layers of the two engine plumes and the plug base form a prism-shaped dome inside which the reverse jet, recirculating flow, aspirating flow, and wall jet (if created) are enclosed. Notice the double-triangle recirculating formation inside the dome is often asymmetric. This is due to a slight difference in the upstream flow environments experienced by the upper- and lower-engine plumes. The highest level of heating occurs on the ramp surface near the thruster outlet. Notice the contours on the upper-engine ramp clearly show the effect and interaction of a 20-thruster plume. The next level of heating occurs on the plug base, especially between the pillows,

where the reverse jet brings in the hot plume gases, torching the surface. The relief comes from an aspirating flow that transports cold inner-base air into the plug base and penetrates as far as the base center. This aspiration is caused by the concentrated pumping effect of the engine plumes. At 0.7 km, this aspiration is strong enough that it entrains the wall jet inwards, before it gets swept away by the engine propulsive flows. Potential afterburning occurs, however, when the air meets the partially combusted hot plume. One outcome of the air aspiration is the cooling of the outside plug base, where a clear demarcation of the heat flux contours is observed. The heating on the plug side wall is caused by the hot engine flow spilling off of the side of the ramp, also known as plume spillage heating. When base bleed is turned on, the injected bleed gas (partially burned hydrogen/oxygen mixture emerges from tiny holes on the pillow) mixes and burns with the aspirated air. The extent of burning depends on the available energy and flow residence time.

At 3.7 km (not shown), due to higher plume expansion, the laterally expanding upper- and lower-engine plume spillages merge into a lateral plume jet that impinges on the outer and offset outer bases, resulting in a higher convective heating (on those bases). Meanwhile, the weakened aspirating flow, due to lower ambient pressure and less concentrated pumping, is still strong enough to entrain the wall jet inward, reaching almost as far as the base center. At 15.3 km (not shown), however, the pumping is too attenuated to induce air aspiration and the plug-base heating reduces drastically. The colder inner-base air is entrained instead by the lateral-moving plume spillages. At 23.4 km, the increased plume spillages are such that the lateral plume jet causes discernible heating on inner, offset outer, and outer bases, as shown in Fig. 3. When impinging on the inner and offset outer bases, portions of the lateral plume jet have no place to go but to go up or down as vertical wall jets. These vertical wall jets may trigger plume-induced flow separation at very high altitudes. On the pillow, wall jets can be seen swirling out laterally but are swept downstream quickly by the main propulsive flow. Similar general base-flow physics continue through an altitude of 31.1 km.

When base bleed is turned on, the aforementioned base-flow physics such as the reverse jet and double-triangle recirculation bubble formation, flow entrainment, plume spillage, plug-base lateral wall-jet formation, offset-outer base vertical wall-jet formation, and lateral plume jet impingement appear similar to those of the baseline cases. However, at altitudes above 15.3 km, the secondary flows immediately downstream from the bleed region are mostly destroyed, possibly caused by the induced bleed flow acceleration.

When a fence is added, the plume spillage is mostly precluded, thereby eliminating the plume spillage heating and the lateral plume jet impingement heating. In addition, the ambient air aspiration that allows afterburning of the recirculated plume inside the plug-base dome is essentially nonexistent. Figure 4 shows the absence of these phenomena. Some wall jets near the end of the plug base (at 23.4 and 31.1 km) manage to penetrate the inner base, or flow over the outer base, but are too weak to cause any significant heating. In summary, these results show that the utilization of a fence has design benefits in terms of plume-induced base-heating reduction, especially on the inner, offset outer, and outer bases. However, the additional heating on the ramp side fence is a potential system issue that may need to be addressed.

Notice in both the base-bleed and base-bleed with fence cases, the bleed gas does not seem to reduce the heating between the pillows (where there are no bleed holes), especially in the subsonic freestream cases. This is possibly caused by the bleed-gas flow direction (flowing straight downstream) and by the reverse jet (to plug-base) impingement that creates a slightly higher center base pressure (than the immediate neighborhood), thereby preventing the bleed gas from reaching that region. Changing bleed-gas flow direction in nearby bleed holes or having bleed gas coming out of the central plug base may reduce the heating load in that region.

Figure 5 shows the computed radiative heat-flux contours at 31.1 km for all three cases in gray scales (0–150). In the baseline case, it can be seen that the influence of the radiative heating is felt over all of the base structures, including the body flap and vertical fin. In the base-bleed case, the computed radiative heat-flux
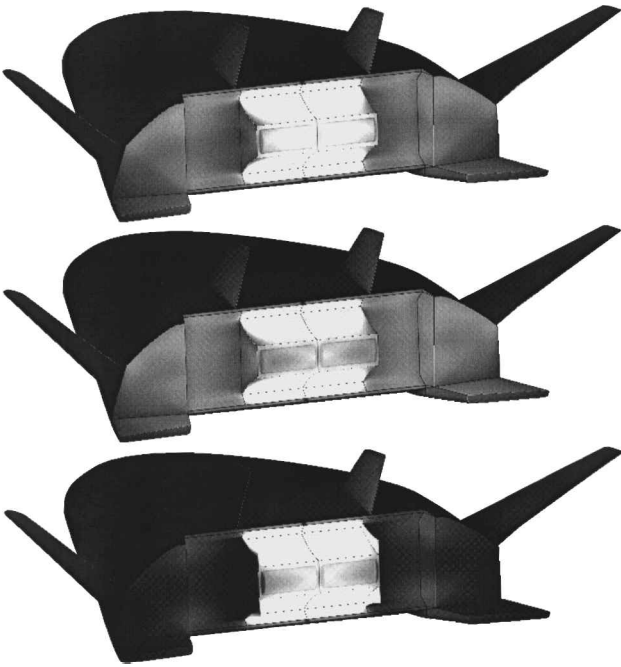
Fig. 5   Radiative heat flux contours at 31.1 km; from top to bottom: baseline, base-bleed, and base-bleed with fence cases.
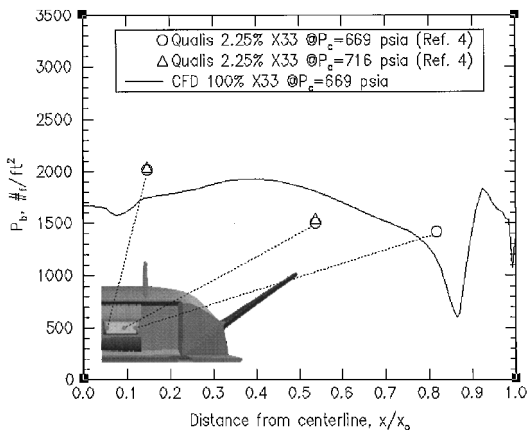

Fig. 6   Comparison of sea-level pillow pressures.

contours are very similar to those of the baseline case except for the plug-base region, where the radiative heating is lowered due to the protective effect of the base bleed. In the base-bleed with fence case, the beam blocking effect by the fence is evident from the drastically reduced irradiation on components from the plug-side wall to outer base, including the body flap. Again, the uniform scale is chosen to accentuate the radiative base-heating physics.

Benchmark with a Subscale Hot-Flow Model Test

In this section, in addition to the results from flight model simulations, results from several additional three-dimensional computations are used to compare with those of 2.25% scaled model hot-fire tests.[4] These additional computations are performed such that the operating conditions match or approximate those of the subscale model test. The subscale model, developed jointly by Qualis Corporation and NASA MSFC, is a simulation of the aft third of the X-33 flight vehicle. The general propulsion system parameters of this subscale model match those of the X-33 (Ref. 4). Details of this short duration hot-flow test can be found in Ref. 5.

Figure 6 shows the comparison of sea-level pillow pressures. The computed base pressures agreed reasonably well with those of the test. The test data shown are averages of transient measurements taken over a 15-ms time period,[4] during which the chamber pressure
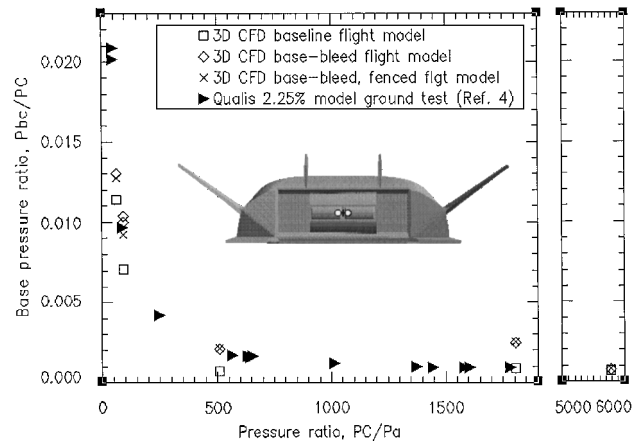

Fig. 7   Comparison of linear aerospike engine base characteristic pressures.

is relatively constant, whereas the predicted curve is bounded by the fluctuations of the measurements (not shown for clarity). The predicted and measured pressure levels indicate that there is a very strong aspiration occurring on the plug base at low altitudes, as shown in Fig. 2.

Figure 7 shows the comparison of base pressure characteristic curves, taken to be the (plug base) central base pressure (taken at the location marked by +) distribution as a function of ambient pressure.[14] It should be noted that the Qualis data were taken at an off-center location, as shown by the circular marks on the pillow. Also, the Qualis tests were performed in a quiescent environment. Still, the predicted baseline characteristic pressures agree reasonably well with those of the tests, indicating the base characteristic pressure is not significantly affected by the freestream flow speed. The predicted base characteristic pressures of the baseline model are generally lower than those of the base-bleed and the base-bleed with fence models, except at PC = 5790 Pa, where the bleed effect is much diluted due to the very high plume expansion. The predicted center base pressures of the base-bleed and fence case are slightly lower than those of the base-bleed only case for pressure ratios lower than 100, possibly due to less aspiration and, thereby, less afterburning. For pressure ratios above 100, there is no discernible difference in central base pressure ratio between the base-bleed case and the base-bleed with fence case. The combined characteristic curves of the test and flight prediction (without base bleed) show that the base wake probably closes, when base-center pressure is not changed by the ambient pressure, at a pressure ratio of approximately 500. The discussion herein indicates the characteristic base pressures predicted by the computational model are reasonable. The effects of base bleed and fence on base characteristic pressures also agree qualitatively with those observed in a cold flow test.[1]

Figures 8–10 show the comparison of predicted base horizontal centerline convective heat fluxes with those of the Qualis 2.25% scaled model tests. The predicted convective heat fluxes of the flight demonstrator (100% X-33) are scaled to those of the 2.25% model according to the scaling law[12]

$$Nu = f(Re^{0.8})$$

where Nu is the Nusselt number and Re represents the Reynolds number.

Figure 8 shows the comparison of base horizontal centerline convective heat fluxes at sea level. The scaled convective heat fluxes compare very well with those of the Qualis test. At sea level with minimal plume expansion, the convective heating is concentrated on the plug base and is almost nil on the inner and outer bases. Furthermore, the convective heating on the pillow for the 2.25% scaled model is more than twice that of the full-scale flight demonstrator. The result is expected from the scaling law.

Figure 9 shows the comparison of base horizontal centerline convective heat fluxes at an approximate altitude of 23.4 km. At this
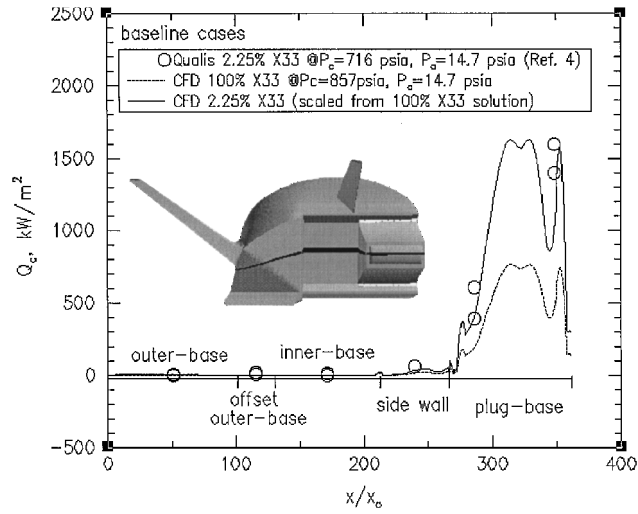
Fig. 8   Comparison of sea-level base horizontal centerline convective heat fluxes.
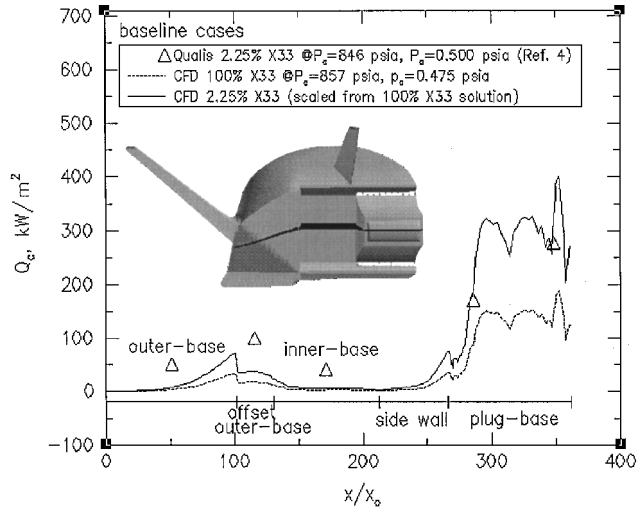

Fig. 9   Comparison of base horizontal centerline convective heat fluxes.
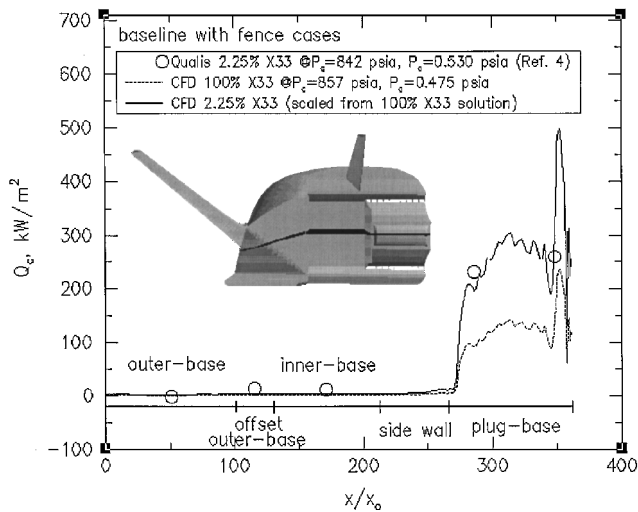

Fig. 10   Comparison of base horizontal centerline convective heat fluxes for baseline with fence.

altitude, the peak heat flux on the pillow is lower (than that of the sea-level case) due to plume expansion and dilution. On the other hand, the heating on the outer bases are higher (than that of the sea-level case) due to the lateral plume jet impingement. The scaled convective heat fluxes compare very well with those of the Qualis test on the plug base, but are somewhat lower than those measured on the outer bases. It is speculated that a slight shedding of the plume under the quiescent condition may have caused the discrepancy.

The effect of a fence on the base horizontal centerline convective heat fluxes is shown in Fig. 10. The scaled convective heat fluxes compare very well with those of the Qualis test. The absence of plume spillage and, thereby, the absence of lateral plume-jet impingement result in negligible heating on the outer bases, as discussed in the preceding section.

In summary, the preceding comparisons demonstrate the accuracy of the computational methodology in terms of predicting the base pressures and convective heat fluxes. These comparisons also confirm the validity of the computed base-heating physics (aspiration, afterburning, reverse-jet and lateral wall-jet formations, plume spillage, and subsequent lateral plume-jet impingement), including the fence effect (plume spillage prevention and plume radiation blocking).

Conclusions

Computational heat transfer analysis is performed to study the effect of fence on linear aerospike plume-induced base-heating physics. The underlying three-dimensional base-heating physics such as aspiration, reverse-jet and wall-jet formations, plume spillage, and lateral plume-jet impingement with the inner- and outer-base surfaces are captured and reflected in the computed base-heating environment. The presence of an engine fence blocks the hot plume radiation and prevents the plume spillage, thereby greatly lessening plume spillage heating and lateral plume-jet impingement heating. The validity of the computational heat transfer methodology is demonstrated by comparing the computed base-flow properties with those of available hot-flow test data.

References

[1]Tomita, T., Takahashi, M., Onodera, T., and Tamura, H., "Effects of Base-Bleed on Thrust Performance of a Linear Aerospike Nozzle," AIAA Paper 99-2586, June 1999.

[2]Huang, D. H., "Aerospike Engine Technology Demonstration for Space Propulsion," AIAA Paper 74-1080, Oct. 1974.

[3]Wang, T.-S., "Analysis of Linear Aerospike Plume-Induced X-33 Base-Heating Environment," *Journal of Spacecraft and Rockets*, Vol. 36, No. 6, 1999, pp. 777–783.

[4]Engel, C. D., "X-33 Base and Aerospike Nozzle Base Environment Hot Firing Test Data," Qualis Corp., QTR 028-4, Huntsville, AL, Sept. 1999.

[5]D'Agostino, M., Seaford, C. M., Engel, C. D., Bender, R., and Engel, B., "Short Duration Base-Heating Test Improvements," International Test and Evaluation Association 1999 Conference, Paper A4, Univ. of Tennessee Space Inst., Tullahoma, TN, Oct. 1999.

[6]Steinbrenner, J. P., Chawner, J. R., and Pouts, C., "Multiple Block Grid Generation in the Interactive Environment," AIAA Paper 90-1602, June 1990.

[7]Davies, C. B., and Venkatapathy, E., "The Multidimensional Self-Adaptive Grid Code, SAGEv2," NASA TM 110350, April 1995.

[8]Chen, Y.-S., "FDNS—A General Purpose CFD Code, Version 4.0," Engineering Sciences, Inc., ESI-TR-97-01, Huntsville, AL, May 1997.

[9]"Injector Design Tool Improvements—Final Technical Report and User's Manual for FDNS V.4.5," Engineering Sciences, Inc., ESI-TR-98-02, Huntsville, AL, April 1998.

[10]Liu, J., Shang, H.-M., Chen, Y.-S., and Wang, T.-S., "GRASP: A General Radiation Simulation Program," AIAA Paper 97-2559, June 1997.

[11] Wang, T.-S., and Luong, V., "Hot-Gas-Side and Coolant-Side Heat Transfer in Liquid Rocket Engine Combustors," *Journal of Thermophysics and Heat Transfer*, Vol. 8, No. 3, 1994, pp. 524–530.

[12] Wang, T.-S., and Chyu, M. K., "Heat Convection in a 180-Deg Turning Duct with Different Turn Configurations," *Journal of Thermophysics and Heat Transfer*, Vol. 8, No. 3, 1994, pp. 596–601.

[13] Wang, T.-S., "Numerical Analysis of Base Flowfield for a Four-Engine Clustered Nozzle Configuration," *Journal of Propulsion and Power*, Vol. 11, No. 5, 1995, pp. 1076–1078.

[14] Wang, T.-S., "Grid-Resolved Analysis of Base Flowfield for Four-Engine Clustered Nozzle Configuration," *Journal of Spacecraft and Rockets*, Vol. 33, No. 1, 1996, pp. 22–29.

[15] Wang, T.-S., and Cornelison, J., "Analysis of Flowfields over Four-Engine DC-X Rockets," *Journal of Spacecraft and Rockets*, Vol. 34, No. 5, 1997, pp. 620–627.

[16] Wang, T.-S., "Delta Clipper-Experimental In-Ground Effect on Base-Heating Environment," *Journal of Thermophysics and Heat Transfer*, Vol. 12, No. 2, 1998, pp. 343–349.

[17] Wang, T.-S., and Chen, Y.-S., "Unified Navier–Stokes Flowfield and Performance Analysis of Liquid Rocket Engines," *Journal of Propulsion and Power*, Vol. 9, No. 5, 1993, pp. 678–685.

[18] Chen, Y.-S., and Kim, S. W., "Computation of Turbulent Flows Using an Extended k–ε Turbulence Closure Model," NASA CR-179204, Oct. 1987.

[19] Wang, T.-S., McConnaughey, P., Chen, Y.-S., and Warsi, S., "Computational Pollutant Environment Assessment from Propulsion System Testing," *Journal of Spacecraft and Rockets*, Vol. 33, No. 3, 1996, pp. 386–392.

[20] Liakopolous, A., "Explicit Representations of the Complete Velocity Profile in a Turbulent Boundary Layer," *AIAA Journal*, Vol. 22, No. 6, 1984, pp. 844–846.

[21] White, F. M., *Viscous Fluid Flow*, McGraw–Hill, New York, 1974, pp. 562–563.

[22] Liu, J., Shang, H.-M., Chen, Y.-S., and Wang, T.-S., "Prediction of Radiative Transfer in General Body-Fitted Coordinates," *Numerical Heat Transfer*, Pt. B, Vol. 31, No. 4, 1997, pp. 423–439.

[23] Svehla, R. A., and McBride, B. J., "FORTRAN IV Computer Program for Calculation of Thermodynamic and Transport Properties of Complex Chemical Systems," NASA TN D-7056, Jan. 1973.